

## MIT Open Access Articles

*Dynamic fragmentation of a brittle plate under biaxial loading: strength or toughness controlled?*

The MIT Faculty has made this article openly available. **Please share** how this access benefits you. Your story matters.

**Citation:** Levy, S., J. F. Molinari, and R. Radovitzky. "Dynamic Fragmentation of a Brittle Plate Under Biaxial Loading: Strength or Toughness Controlled?" *Int J Fract* 174, no. 2 (April 2012): 203–215.

**As Published:** <http://dx.doi.org/10.1007/s10704-012-9691-5>

**Publisher:** Springer Science+Business Media

**Persistent URL:** <http://hdl.handle.net/1721.1/86189>

**Version:** Author's final manuscript: final author's manuscript post peer review, without publisher's formatting or copy editing

**Terms of use:** Creative Commons Attribution-Noncommercial-Share Alike



# Dynamic fragmentation of a brittle plate under biaxial loading: strength or toughness controlled?

S. Levy<sup>1</sup>, J. F. Molinari<sup>1\*</sup>, R. Radovitzky<sup>2</sup>

<sup>1</sup>LSMS–IIC–ENAC

Ecole Polytechnique Fédérale de Lausanne, 1015 Lausanne, Switzerland

<sup>2</sup>Department of Aeronautics and Astronautics

Massachusetts Institute of Technology, Cambridge, MA 02139, United States

\* Corresponding author: jean-francois.molinari@epfl.ch

---

**Abstract** — The fragmentation of a brittle plate subjected to dynamic biaxial loading is investigated via numerical simulations. The aim is to extend our understanding of the dynamic processes affecting fragment size distributions. A scalable computational framework based on a hybrid cohesive zone model description of fracture and a discontinuous Galerkin formulation is employed. This enables large-scale simulations and, thus, the consideration of rich distributions of defects, as well as an accurate account of the role of stress waves. We study the dependence of the fragmentation response on defect distribution, material properties, and strain rate. A scaling law describing the dependence of fragment size on the parameters is proposed. It is found that fragmentation exhibits two distinct regimes depending on the loading rate and material defect distribution: one controlled by material strength and the other one by material toughness. At low strain rates, fragmentation is controlled by defects, whereas at high strain rates energy balance arguments dominate the fragmentation response.

**Keywords:** Biaxial tension, discontinuous Galerkin, cohesive zone model, parallel computing, defects, energy balance, stress waves

---

## 1 Introduction

The dynamic fragmentation of brittle solids under intense loading continues to be a subject of significant scientific and practical interest. One of the main challenges is the prediction of the distribution of fragment sizes for general fragmentation events which encompass a vast range of length scales, material properties, structural dimensionality, and loading conditions. Extensive experimental studies have provided a vast body of data of fragment size distributions [9, 20] for particular configurations. Analytical and statistical theories accounting for specific relevant mechanisms such stress wave propagation [12] and energy balance [5, 6] have been successful at predicting experimentally observed characteristic fragment sizes. A recent book [8] provides a comprehensive survey of the statistical and energy-based theories of fragmentation as they apply to rings and shells.

For more general fragmentation events and for a full consideration of the physics of the problem, it has become customary to resort to computer simulation, [2, 22, 19, 23, 24, 10]. Numerical approaches aim to describe all the relevant physical mechanisms of the fragmentation event, which remain not well understood. This includes the temporal evolution of the stress waves within the material, crack nucleation, propagation, branching and coalescence leading to the formation of fragments.

The first challenge in describing a fragmentation event is to determine the location within the material where failure is more likely to initiate. In brittle materials, this normally occurs at defects such as pores, inclusions, grain boundary and triple points which act as stress concentration sites leading to the nucleation of cracks. The location, density, and size of defects thus govern crack initiation. As pointed out by Mott during World War II, stress waves also play a prevailing role [13]. Mott developed a well-known experiment, which consists in expanding a ring circumferentially until it fails [12]. Owing to the one-dimensional geometry of the ring, the only operative failure in this test is crack initiation. This provided deep understanding of the role of crack initiation on the dynamics of fragmentation. Mott explained that, when a crack initiates, a release stress wave emanates from the new free surface and propagates circumferentially along the ring, unloading the surrounding material and protecting it from further damage [13]. Denoual et al. [3] based their statistical theory of brittle fragmentation on this protected zone idea.

A second difficulty is the prediction of crack paths. In multi-dimensional structures, cracks propagate and branch until they reach a free surface at the external boundary of the body or at another crack surface, or until the stress intensity factor at its tip falls below a critical threshold. The evolution of a crack is strongly influenced by its surroundings. Indeed, the stress field in the neighborhood of the crack tip, which governs crack propagation, depends upon the stress waves released by other cracks, as well as on the presence of local defects. As a result, fragmentation of multi-dimensional structures is governed by a complex network of interacting stress waves and by material microstructure.

The purpose of this study is to investigate the role of stress waves and material properties in dynamic fragmentation processes in brittle plates subject to biaxial loading at a wide range of strain rates. Toward this end, we employ an advanced computational framework based on a discontinuous Galerkin formulation of the continuum problem [15, 16] and Cohesive Zone Models of fracture [17]. Although the structure and the applied loading considered are bi-dimensional, out-of-plane responses resulting from the fragmentation process are fully accounted for in the three dimensional numerical framework. We show that, although material properties and loading rate significantly influence the average fragment size, a unique characteristic response of the plate fragmentation exists. We also compare the numerical results to analytical models based on energy balance arguments [6], which helps to explain the role of the additional governing mechanisms controlling fragmentation at low and high strain rates neglected in simplified models.

The mesh convergence of the fracture energy and fragment size distributions has long been a recognized issue in the numerical simulation of dynamic fragmentation [11]. That study showed the need for high mesh resolution in the unidimensional case. A unique advantage of this simulation capability is its inherent parallel scalability, which enables large-scale simulation of dynamic fragmentation and thus to obtain converged results. The study presented here also furnishes, as a sideline, a three-dimensional convergence study of dynamic fragmentation at high loading rates.

In the next section we briefly summarize the main features of the discontinuous Galerkin, Cohesive Zone Model formulation and its scalable numerical implementation. Section three provides a detail description of the driver numerical test for the dynamic fragmentation study, consisting in the dynamic bi-axial tensile loading of a thin plate for a large range of strain rates from quasi-static to very highly dynamic loadings. Section four is devoted to studying the numerical convergence of the simulations where it is shown that the number of fragments and the distribution of fragment masses are independent of the mesh if the element size is sufficiently small. In section five, the evolution of the average fragment size with strain rate and material parameters is investigated. We compare our results to prior one-dimensional numerical results [10], as well as analytical energy models [5, 6] in order to underline their limitations. Finally, in section six, we expose the reasons

for these limitations, and provide a discussion summarizing the physical mechanisms that operate during dynamic fragmentation.

## 2 Numerical framework

### 2.1 The hybrid discontinuous Galerkin - Cohesive Zone Model formulation

#### 2.1.1 Motivation

We adopt the scalable framework for modeling dynamic fracture and fragmentation of solids in three dimensions presented in [17, 18]. The method is based on a combination of a discontinuous Galerkin (DG) formulation of the continuum problem and the Cohesive Zone Model of fracture, hereinafter referred to as CZM. Prior to fracture, the flux and stabilization terms arising from the DG formulation at inter-element boundaries are enforced via interface elements, much like in the conventional intrinsic cohesive element approach, albeit in a way that guarantees consistency and stability. Upon the onset of fracture, the traction-separation law governing the fracture process, hereinafter referred to as TSL, becomes operative without the need to insert a new cohesive element.

The main advantage of the method is that it avoids the need to propagate topological changes in the mesh as cracks and fragments develop, which enables the indistinctive treatment of crack propagation across processor boundaries and, thus, the scalability in parallel computations. Another advantage of the method is that it preserves consistency and stability in the uncracked interfaces, thus avoiding issues with wave propagation typical of intrinsic cohesive element approaches.

For completeness, we summarize the main steps of the formulation in the following.

#### 2.1.2 Weak formulation

Let us consider the dynamic motion of a body, whose reference configuration is  $\Omega_0$  at time  $t_0$ . At any time  $t$  in  $T = [t_{initial}, t_{final}]$ , the position  $\mathbf{x}$  of the material point  $\mathbf{X}$  is described by the deformation mapping:

$$\mathbf{x} = \boldsymbol{\varphi}(\mathbf{X}, t) \quad \forall \mathbf{X} \in \Omega_0, \forall t \in T \quad (1)$$

Its boundary surface  $\partial\Omega_0$  is partitioned into a Dirichlet part  $\partial_D\Omega_0$ , a Neumann part  $\partial_N\Omega_0$ , and an internal boundary  $\partial_I\Omega_0$ , such that  $\partial\Omega_0 = \partial_D\Omega_0 \cup \partial_N\Omega_0 \cup \partial_I\Omega_0$  and  $\partial_D\Omega_0 \cap \partial_N\Omega_0 \cap \partial_I\Omega_0 = \emptyset$ .  $\partial_I\Omega_0$  can either represent a physical discontinuity (such as a fracture surface) or a numerical discontinuity (such as the boundary between two elements of the mesh).

At an internal boundary  $\partial_I\Omega_0$ , the *jump*  $\llbracket \bullet \rrbracket$  and the *average*  $\langle \bullet \rangle$  operators are defined as:

$$\llbracket \bullet \rrbracket = \bullet_2 - \bullet_1 \quad \langle \bullet \rangle = \frac{\bullet_2 + \bullet_1}{2} \quad (2)$$

The weak formulation of the hybrid discontinuous Galerkin - CZM is [17, 18]:

$$\begin{aligned} & \int_{\Omega_0} (\rho_0 \dot{\boldsymbol{\varphi}} \delta\boldsymbol{\varphi} + \mathbf{P} : \nabla_0 \delta\boldsymbol{\varphi}) dV + \alpha \left( \int_{\partial_I\Omega_0} \mathbf{T}(\llbracket \boldsymbol{\varphi} \rrbracket) \llbracket \delta\boldsymbol{\varphi} \rrbracket dS \right) \\ & + (1 - \alpha) \left( - \int_{\partial_I\Omega_0} \langle \mathbf{P} \rangle \llbracket \delta\boldsymbol{\varphi} \rrbracket \mathbf{N} dS + \int_{\partial_I\Omega_0} \llbracket \boldsymbol{\varphi} \rrbracket \otimes \mathbf{N} : \left\langle \frac{\boldsymbol{\beta}}{h_s} \mathbf{C} \right\rangle : \llbracket \delta\boldsymbol{\varphi} \rrbracket \otimes \mathbf{N} dS \right) \\ & = \int_{\partial_N\Omega_0} \bar{\mathbf{T}} \delta\boldsymbol{\varphi} dS \quad \forall \delta\boldsymbol{\varphi} \in \mathbf{B}_X^0, \forall t \in T \end{aligned} \quad (3)$$

In this expression,  $\mathbf{P}$  is the first Piola-Kirchhoff stress tensor,  $\beta$  a stabilization parameter ( $\beta > 0$ ),  $h_s$  the element characteristic length,  $\mathbf{N}$  the unit normal to the reference configuration, and  $\mathbb{C}$  the tangent material modulus.  $\mathbf{T}$  is the cohesive traction, which is function of the jump in displacements across the interface and is responsible for describing the fracture process. Following [16], in the simulations we adopt  $\beta = 4$ .

It can be observed that in the dG-CZM formulation, in addition to the classic terms corresponding to the Principle of Virtual Work, surface integrals on the internal boundary  $\partial_I \Omega_0$  appear. Prior to fracture ( $\alpha = 0$ ), the simulation proceeds according to the prescription of the DG terms which enforce compatibility and equilibrium at interelement boundaries in a weak manner. Upon the onset of fracture, the TSL describing the fracture process becomes operative ( $\alpha = 1$ ). Another difference of the dG-CZM and the original CZM is that the fracture criterion is evaluated directly at the interelement boundary as opposed to the bulk element quadrature points. In addition, the dG-CZM formulation allows for partially-cracked interface elements, where one or more quadrature points satisfy the fracture criterion and the TSL becomes operative, and where the remaining quadrature points remain uncracked. This affords purely-local sub-grid resolution of emerging cracks.

### 2.1.3 Traction-Separation Law (TSL)

In this work we adopt the Camacho and Ortiz [1] linear irreversible law. It relates the cohesive stress  $\sigma_{coh}$  and the crack tip opening  $\delta_{coh}$ .  $\sigma_{coh}$  is defined by the norm of the cohesive traction  $\mathbf{T}$ , while  $\delta_{coh}$  is expressed by:

$$\delta_{coh} = \sqrt{\delta_n^2 + \gamma^2 \delta_t^2} \quad (4)$$

$\delta_n$  and  $\delta_t$  are respectively the normal and tangential parts of the displacement jumps across the interface  $[[\varphi]]$ . The parameter  $\gamma$  balances the tension and shear contributions. In the simulations, we take  $\gamma = 1$ .

Denoting the cohesive strength  $\sigma_c$  and the critical opening  $\delta_c$ , the cohesive stress  $\sigma_{coh}$  behaves by following:

$$\frac{\sigma_{coh}}{\sigma_c} = 1 - \frac{\delta_{coh}}{\delta_c}, \text{ for } \delta_{coh} > 0, \delta_{coh} = \delta_{max} \text{ and } D < 1 : \text{ opening} \quad (5)$$

$$\frac{\sigma_{coh}}{\sigma_c} = 1 - \frac{\delta_{max}}{\delta_c}, \text{ for } \delta_{coh} < \delta_{max} \text{ and } D < 1 : \text{ closing and reopening} \quad (6)$$

The local damage  $D$  is related to the maximum opening. Its value is between zero and one (respectively referring to null damage and complete failure):

$$D = \min \left( \frac{\delta_{max}}{\delta_c}, 1 \right) \quad (7)$$

The cohesive energy is the area under the curve. When fracture is complete, it is equal to the toughness  $G_c = \frac{\sigma_c \delta_c}{2}$ .

### 2.1.4 Numerical implementation

It is rather straightforward to update a usual finite element code to get to the present hybrid implementation. The main technical difference lies in the definition of a suitable internal boundary. When the initial domain is partitioned into  $E$  elements  $\left( \Omega_0 \approx \Omega_{0h} = \bigcup_{e=1}^E \Omega_0^e \right)$ , the interior

boundary  $\partial_I \Omega_0$  can be composed of all the boundaries between elements:

$$\partial_I \Omega_0 = \left( \bigcup_{e=1}^E \partial \Omega_0^e \right) \setminus \partial \Omega_{0h} \quad (8)$$

The discretization in space commonly gives:

$$\mathbf{M} \ddot{\mathbf{x}} + \mathbf{R}^{int}(\mathbf{x}) = \mathbf{R}^{ext}(x) \quad (9)$$

where  $\mathbf{R}^{int}$  and  $\mathbf{R}^{ext}$  are internal and external force arrays,  $\mathbf{M}$  is the lumped mass matrix and  $\mathbf{x}$  is the nodal coordinate array.  $\mathbf{R}^{int}$  embodies the terms of both the discontinuous Galerkin and the cohesive formulations.

Furthermore, the discretization in time is a conventional explicit integration. A second-order central difference scheme with mass lumping is adopted. A condition on the time step is required to guarantee stability:

$$\Delta t \leq \Delta t_{cr}, \text{ with } \Delta t_{cr} = \frac{1}{(c \beta)^{1/2}} \min_{e=1}^E (h_e) \quad (10)$$

where  $\beta$  is the stabilization parameter of the discontinuous Galerkin formulation,  $c$  is the wave speed, and  $h_e$  is the characteristic dimension of element  $e$ .

### 3 Definition of the problem

#### 3.1 Description of the test

We consider a thin square plate of dimension  $L_{plate} = 10 \text{ cm}$  and thickness  $0.15 \text{ mm}$ . The value of the thickness is modified when appropriate to the element size to ensure the good quality of the mesh. Since the plate remains very thin in all the simulations, varying the thickness does not affect the fragmentation pattern. The material properties used as baseline in simulations correspond to aluminum oxide AD-995: Young's modulus  $E = 370 \text{ GPa}$ , Poisson ratio  $\nu = 0.22$ , volumetric mass  $\rho = 3900 \text{ kg.m}^{-3}$ , static failure strength  $\sigma_c = 262 \text{ MPa}$  and toughness  $G_c = 50 \text{ N/m}$ . These parameters will be modified in the following sections in order to understand their influence on the fragmentation process (c.f. table 1). The plate is subjected to biaxial tension during the entire duration of the test (figure 1(a)). Initial displacements and velocities are such that the plate undergoes uniform expansion with no initial propagating stress waves. We vary the strain rate from  $10 \text{ s}^{-1}$  to  $10^5 \text{ s}^{-1}$ . These boundary conditions lead to the fragmentation of the plate, as displayed in figure 1(b).

#### 3.2 Modeling of material heterogeneity and parametric studies

Every material is inherently heterogeneous. It may contain pores, inclusions, grain boundaries, crystal imperfections, which we will collectively refer to as defects. Since they have tendency to concentrate stresses, these defects are favorable locations for fracture initiation. Experimental evidence [21] has shown that the failure strength of most materials follows a Weibull distribution. We associate the failure strength of a defect to the cohesive strength of its associated cohesive element. The distribution of cohesive strengths is thus given by:

$$F(\sigma_c) = 1 - e^{-\left(\frac{\sigma_c - \sigma_{c,min}}{\lambda}\right)^m} \quad (11)$$

$\sigma_{c,min}$  is the minimum cohesive strength, which corresponds to the quasi-static failure strength.  $m$  is a material parameter called Weibull modulus.  $\lambda$  is the scale parameter, and depends on the

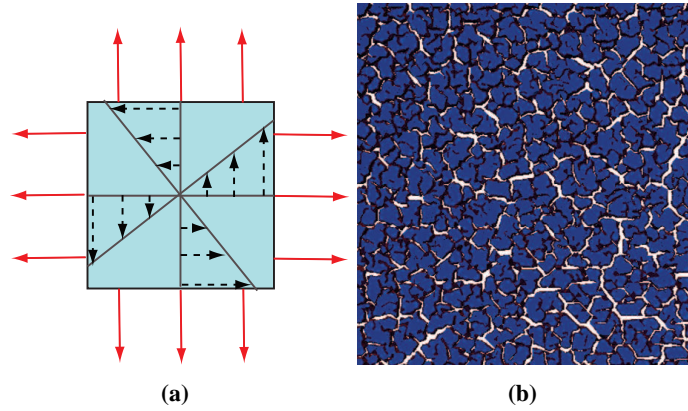


Figure 1: (a) Plate under biaxial tension. Dashed arrows indicate the extent of initial velocity amplitudes. Plain arrows indicate boundary conditions in displacements. (b) Fragmented plate from which we can extract fragment masses.

material and on the geometry of the structure. In the present paper, we have tested the response of several distributions of defects plotted in figure 2.

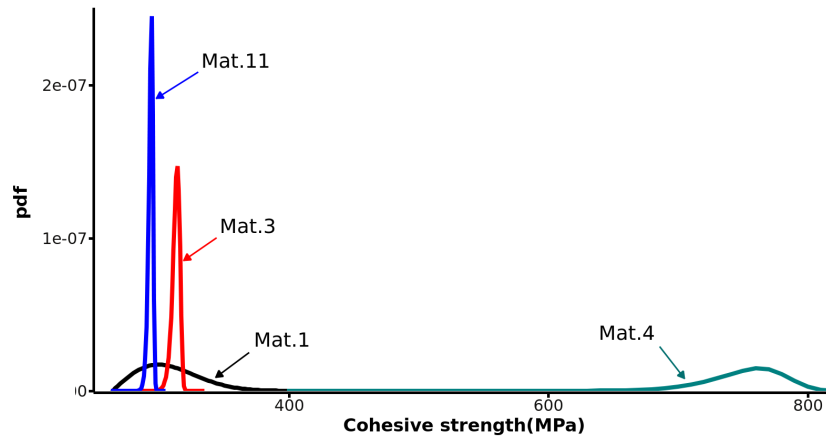


Figure 2: Probability density function of some of the distributions of cohesive strengths studied (see table 1).

As part of the study, we also vary material parameters (Young's modulus, volumetric mass, toughness). Table 1 details each set of parameters used in the simulations.

## 4 Numerical convergence

We first verify the validity of the computed results through a convergence study. In the case of fragmentation, convergence can either concern the number of fragments or the distribution of fragment sizes. Reaching convergence may, however, be technically challenging since fine meshes are usually required to capture the smallest fragments. We benefit from the efficiency of the parallel implementation that the formulation detailed in section 2 provides. Running codes on many processors allows us to increase the degrees of freedom significantly and obtain converged results at high strain rates (up to  $10^5/s$ ).

	Young's modulus (GPa)	Volumetric mass ( $kg/m^3$ )	Toughness (N/m)	$\sigma_{c,min}$ (MPa)	Weibull modulus	Scale parameter (MPa)
Mat.1	370	3900	50	264	2	50
Mat.2	275	3750	50	264	2	50
Mat.3	260	3690	50	299	20	50
Mat.4	260	3690	50	305	2	500
Mat.5	370	3900	250	264	2	50
Mat.6	370	3900	50	104	2	50
Mat.7	600	3900	50	264	2	50
Mat.8	370	6327	50	264	2	50
Mat.9	370	1054	50	264	2	50
Mat.10	370	3900	50	69	2	50
Mat.11	370	3900	50	284	20	30

Table 1: Material parameters used in the simulations

A plate made of aluminum oxide AD-995 with nearly no defects (Mat.11 in table 1) is meshed with 8.000 to 6.000.000 degrees of freedom. We compute the average fragment size and distribution of fragment masses. Figure 3 displays the evolution of the number of fragments with degrees of freedom, obtained for  $\dot{\epsilon} = 10^4 s^{-1}$ , in two cases: with and without dust. We name dust the fragments composed of one or two tetrahedra, to prevent the element size to determine fragment size. To compare numerical results to experiments, this elimination would be necessary, since techniques used to measure fragment sizes, have a minimum size that can be resolved. The curves in figure 3 first increase, suggesting that every edge of the mesh is at least damaged. Then, they slightly decrease until reaching their final value. Some edges of the mesh are broken, others are damaged or intact. Convergence in terms of number of fragments is thus achieved for meshes with at least 200000 degrees of freedom. To the best of our knowledge, convergence has been reached in one dimension [11], but this is the first attempt of fragment convergence in three dimensions.

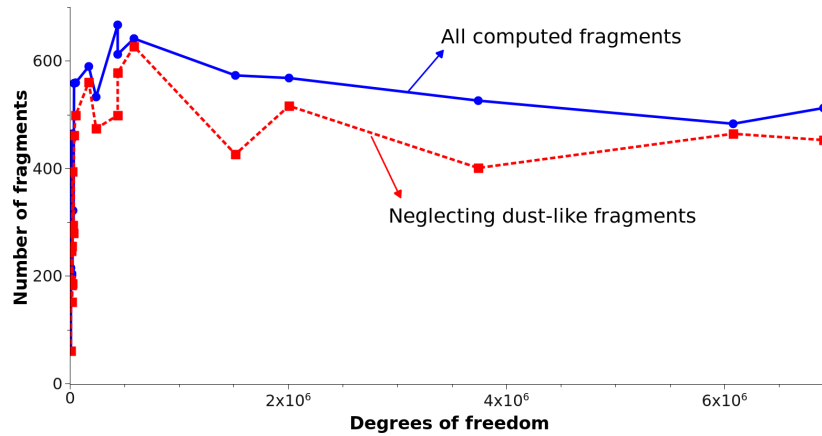


Figure 3: Evolution of the number of fragments with the degrees of freedom, for the strain rate  $\dot{\epsilon} = 10^4 s^{-1}$ .

Besides, distribution of fragment masses can also be made independent from the mesh if dust is neglected. Figure 4 plots the inverse of the cumulative density function of the normalized fragment masses in two cases: accounting for all the fragments, and neglecting dust. Note that, in figure 4, the x-axis involves the average fragment mass in order to compare only the shape of



distribution of fragment mass (and not the number of fragments, already shown previously). When dust is included in the statistics, the curves do not superimpose, whereas they are very close if dust is neglected. This observation suggests that the shape of the distribution of fragment masses is substantially more sensitive to dust than to mesh fineness.

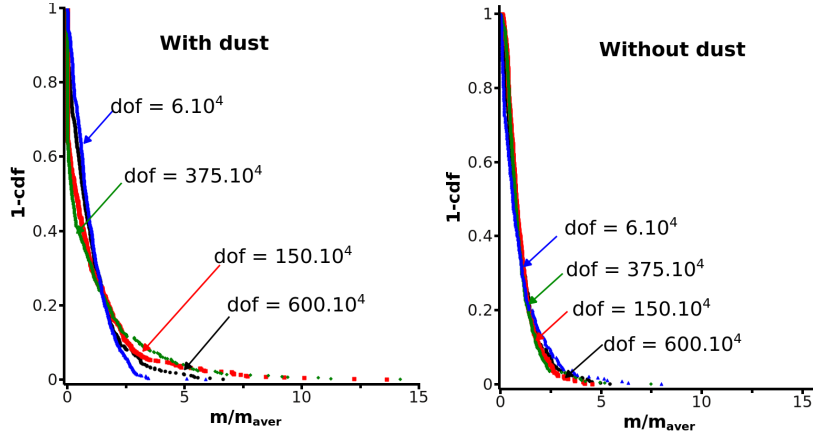


Figure 4: Inverse of the cumulative density function of the fragment mass in two cases: with and without accounting for dust (fragments composed of one or two tetrahedra). The x-axis is normalized by the average fragment mass. Strain rate is  $\dot{\epsilon} = 10^4 \text{ s}^{-1}$ .

In summary, for fine enough meshes, the number of fragments and the shape of the fragment mass distribution are independent from the number of degrees of freedom. We also computed the energy dissipated into failure and observed that fine meshes are associated to dissipative features independent of the number of degrees of freedom. All the results that will be presented in the following sections were computed on sufficiently fine meshes, to obtain converged values.

## 5 Evolution of the average fragment size with strain rate

Material parameters strongly influence the fragmentation behavior. To underline it, we conducted several simulations using the materials referenced in table 1. Figure 5 shows the average fragment size  $s_{aver}$  for several strain rates. It exhibits an obvious dependence with respect to both strain rate and material parameters.

In this section, we investigate if there exists a way of scaling these scattered points in order to gather them into a representative curve. We define the normalized strain rate and the normalized average fragment size:

$$\bar{\dot{\epsilon}} = \frac{\dot{\epsilon}}{\dot{\epsilon}_{ch}} \text{ and } \bar{s} = \frac{s_{aver}}{s_{ch}} \quad (12)$$

where  $\dot{\epsilon}_{ch}$  is the characteristic strain rate and  $s_{ch}$  is the characteristic fragment size. Initially,  $\dot{\epsilon}_{ch}$  and  $s_{ch}$  were derived for homogeneous materials with unique cohesive strength  $\sigma_c$  [4, 24]:

$$\dot{\epsilon}_{ch} = \frac{\sigma_c^3 c}{E^2 G_c} \text{ and } s_{ch} = \frac{G_c E}{\sigma_c^2} \quad (13)$$

Predictions of the average fragment size for such homogeneous materials have been proposed by Grady [6] and Glenn and Chudnovsky [5], who based their models on energy balance arguments. In his key paper [6], by equating local kinetic energy and fracture energy, Grady establishes a

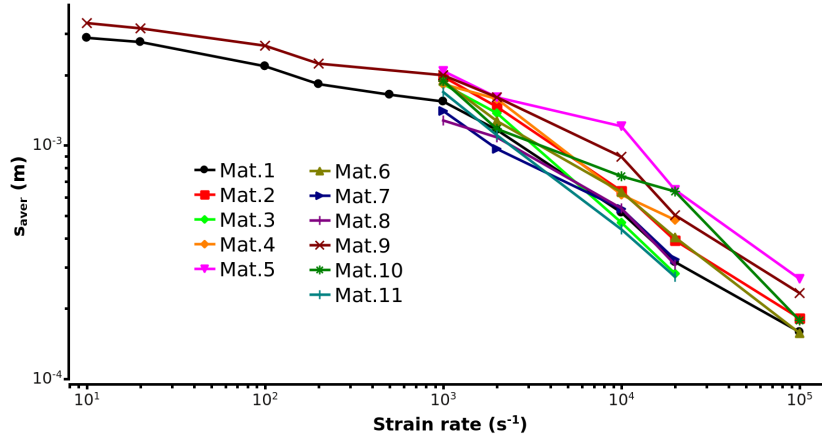


Figure 5: Average fragment size evolving with strain rate in log-log axes. Nine materials are fragmented over the range  $\dot{\epsilon} = 10^3 s^{-1}$  to  $\dot{\epsilon} = 10^5 s^{-1}$ , and two materials are fragmented over the range  $\dot{\epsilon} = 10 s^{-1}$  to  $\dot{\epsilon} = 10^5 s^{-1}$ . Material parameters are detailed in table 1.

general expression of the fragment's characteristic length scale in dynamics. In two dimensions, it is:

$$\bar{s}_{Gr} = \left( \frac{24}{\bar{\dot{\epsilon}}^2} \right)^{1/3} \quad (14)$$

Glenn and Chudnovsky [5] generalized Grady's derivation to quasi-static loadings. Potential energy is prevailing in quasi-static, whereas kinetic effects are dominant in dynamics. They wrote the balance between potential, kinetic, and failure energy at the fragment scale. It led to an analytical expression of the average fragment size whose representative curve is displayed in figure 6.

Recently, using expanding ring numerical tests, Levy and Molinari [10] generalized these expressions to heterogeneous materials:

$$\dot{\epsilon}_{ch} = \frac{\sigma_{c,aver}^3 c}{E^2 G_c} \text{ and } s_{ch} = \frac{G_c E}{\sigma_{c,aver}^2} f(\text{defects}) \quad (15)$$

where  $\sigma_{c,aver}$  is the average of the cohesive strengths,  $c$  the wave velocity,  $E$  the Young's modulus, and  $G_c$  the toughness. The function  $f(\text{defects})$  is a semi-empirical function, expressed as the product of two independent functions  $f_1$  and  $f_2$ . The first function  $f_1$  is associated to the shape of the cohesive strength distribution. It quantifies the effect of stress wave interactions. For instance, when the left tail has an infinite slope (such as the uniform distribution), numerous cracks initiate simultaneously when the stress reaches the weakest link's strength  $\sigma_{c,min}$ . This leads to a rapid response during which stress waves barely interact; many fragments are generated independently. On the contrary, when the left tail has a null slope (such as the normal distribution), cracks are initiated smoothly, one after the other. Stress waves have time to interact and to release the structure; fewer fragments are generated. Therefore, similarly as the fragment size  $s_{ch}$ , which is inverse proportional to the number of fragments,  $f_1$  is a decreasing function of the left tail's slope of the cohesive strength distribution. Empirical arguments have shown that  $f_1$  is comprised between 1 and  $\sqrt{2}$  [10]. The second function  $f_2$  is a decreasing function of the ratio between  $\sigma_{c,aver} - \sigma_{c,min}$  and  $\sigma_{c,aver}$ , and is comprised between 0 and 1. It quantifies the amount of breakable defects. Given the peak stress  $\sigma_{peak}$ , the maximum number of defects that may break is the probability of finding a cohesive strength smaller than peak stress times the number of defects. For instance, while peak stress remains lower than  $\sigma_{c,aver}$ , two distributions with the same  $\sigma_{c,aver}$  may not result in the same

number of fragments. Distributions with large standard deviation may generate many small fragments because they contain more breakable defects. Hence,  $f_2$ , and a fortiori  $s_{ch}$ , are decreasing with  $\sigma_{c,aver} - \sigma_{c,min}$ . To summarize, the function  $f(\text{defects})$  conveys the idea that variations of the tail of the left slope of the distribution of cohesive strengths yield distinct fragmentation behavior, and that the minimum and the average cohesive strengths constrain the maximum number of breakable defects.

Thereafter, Levy and Molinari [10] proposed a unique empirical law to describe the evolution of the normalized average fragment size with normalized strain rate for one-dimensional fragmentation:

$$\bar{s} = \frac{3}{1 + 4.5 \bar{\dot{\epsilon}}} \quad (16)$$

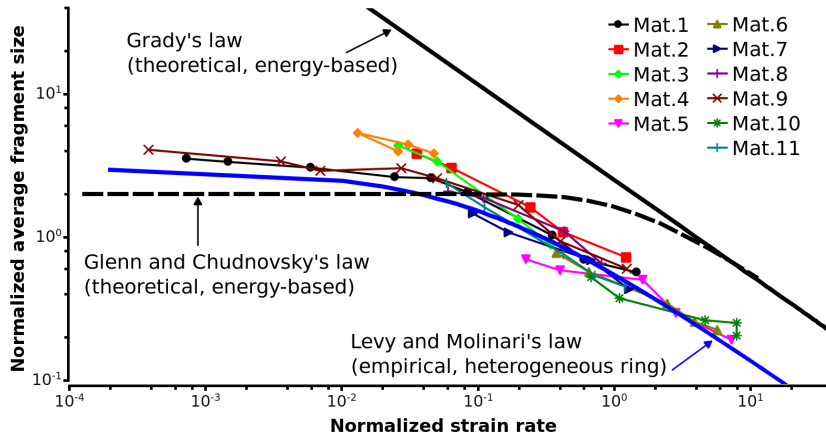


Figure 6: Normalized average fragment size  $\bar{s}$  function of normalized strain rate  $\bar{\dot{\epsilon}}$  in log-log axes. Comparison of the present results to Grady's, Levy and Molinari's, and Glenn and Chudnovsky's models. The scaling is defined by equation 15.

Figure 6 displays these three models, along with numerical results for the plate under biaxial tension. The scaling defined in one-dimension brings all the computed values into a reasonably narrow range. Hence, the present numerical study extends the validity of equation 15 to quasi two-dimensional fragmentation of heterogeneous materials subjected to tensile loadings.

By contrast, our computed values do not precisely follow energetic estimates. Apart from the fact that we interestingly recover the  $-2/3$  power law exponent (equation 14), figure 6 highlights significant differences. In quasi-statics, the average fragment size is about twice Glenn and Chudnovsky's predictions [5], whereas it is lower by a factor of two than Grady's characteristic size in dynamics. These major differences are due to energetic and dynamics effects. Experimental evidence [7] suggests that Grady's prediction overestimates the actual fragment size, therefore conforing our numerical simulations.

In the following, we describe the physical mechanisms governing the low and high strain rate responses, and emphasize the main reasons why energy models do not predict the average fragment size as accurately as numerical simulations.

## 6 Strength and toughness controlled regimes

### 6.1 Some limitations of the energy balance arguments

Let us first derive the basic energy arguments, based on Grady's and Glenn and Chudnovsky's interpretations. A fragment is supposed to be square-shaped with dimension  $s$ . We assume linearity before failure. At the time of failure, the stress within the fragment is  $\sigma_{peak}$  and the associated volumetric energies are:

$$e_{pot} = \frac{\sigma_{peak}^2}{2E} \quad (17)$$

$$e_{kin} = \frac{\rho \dot{\epsilon}^2 s^2}{12} \quad (18)$$

$$e_{\Gamma} = \frac{2G_c}{s} \quad (19)$$

$e_{pot}$ ,  $e_{kin}$  and  $e_{\Gamma}$  are respectively the volumetric potential, kinetic, and failure energies.

At low strain rates, kinetic energy is negligible. Potential energy prevails, and the size of the fragment is:

$$e_{pot} = e_{\Gamma} \Rightarrow s_{QS} = \frac{4G_c E}{\sigma_{peak}^2} \quad (20)$$

By contrast, at high strain rates, potential energy is negligible, and kinetic energy controls the process. Fragment size is the one derived by Grady in equation 14:

$$e_{kin} = e_{\Gamma} \Rightarrow s_{DY} = \left( \frac{24G_c}{\rho \dot{\epsilon}^2} \right)^{1/3} \quad (21)$$

The transition between the quasi-static and the dynamic regimes occurs at the strain rate  $\dot{\epsilon}_{TR}$  such that:

$$s_{DY} = s_{QS} \Rightarrow \dot{\epsilon}_{TR} = \sqrt{\frac{3\sigma_{peak}^3 c}{8E^2 G_c}} \quad (22)$$

$\dot{\epsilon}_{TR}$  defines the limit between the quasi-static and the dynamic regimes, that are respectively governed by potential and kinetic energies. One should note the correspondences with the scaling parameters defined in section 5. The characteristic strain rate  $\dot{\epsilon}_{ch}$  is proportional to  $\dot{\epsilon}_{TR}$ , and the characteristic size  $s_{ch}$  has a form close to  $s_{QS}$ . Relations 20 and 21 thus constitute a physical interpretation of the scaling.

To verify whether these expressions are valid, we compare them to numerical simulations. Figure 7(a) represents the evolution of the average fragment size with strain rate for materials Mat.1 and Mat.9 (see table 1), along with the theoretical sizes  $s_{QS}$  and  $s_{DY}$ . To get a plot independent from material parameters, we normalize the strain rate by  $\dot{\epsilon}_{TR}$ , and the fragment size by  $s_{QS}$ . Figure 7 underlines that the energy arguments provide good general trends. However, they do not predict accurately the value of transition  $\dot{\epsilon}_{TR}$ , and the average fragment size  $s_{aver}$ : at low strain rates, we compute  $s_{aver} \geq s_{QS}$ , whereas at high strain rates,  $s_{aver} \leq s_{DY}$ . More precisely, for the specific example displayed in figures 7, we observe that  $s_{aver} \simeq 2s_{QS}$  and  $s_{aver} \simeq s_{DY}/2$  (figure 7(b)). It suggests that only half of the potential energy is converted into failure energy at low strain rates, and that four times the local kinetic energy is consumed in failure at high strain rates. It appears

that another source of energy provides additional energy to complete fragmentation. These observations underline the limitations of the energy arguments. The physical mechanisms involved in energy transfers are more complex than simple energy conversions. Numerical simulations have the ability to track the time evolution of the energies, and allow us to access more details. In the following section, we explain the origins of these limitations raised by energy models, and describe qualitatively the energetic and dynamic processes involved in fragmentation.

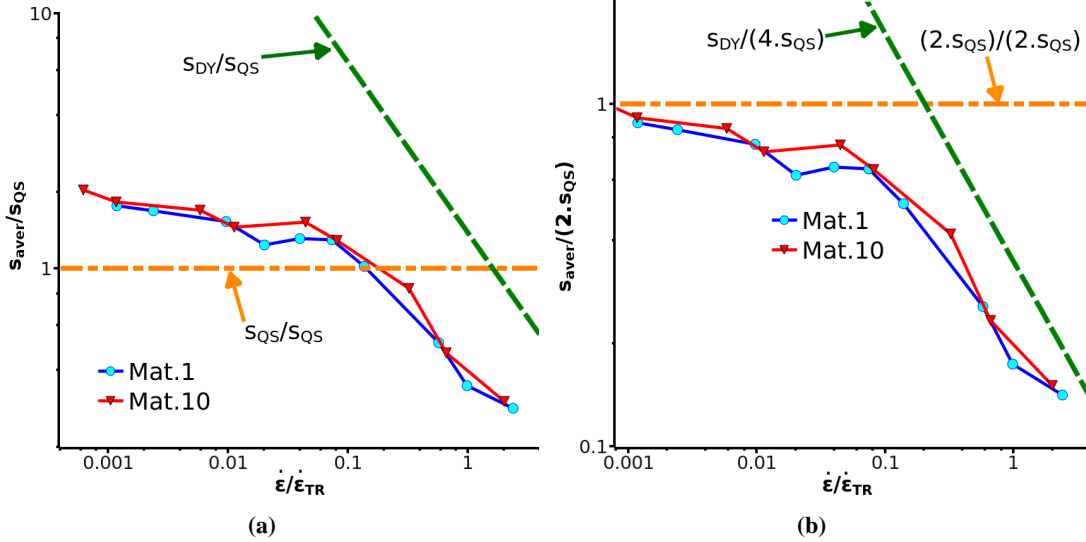


Figure 7: Fragment sizes evolving with strain rate in log-log axes for materials Mat.1 and Mat.9 (table 1).  $s_{aver}$  is the computed average fragment size,  $s_{QS}$  and  $s_{DY}$  are the theoretical quasi-static and dynamic sizes. (a) Energy models only provide trends. (b) With adequate rescaling of  $s_{QS}$  and  $s_{DY}$ , we can deduce empirically the proportion of energy used in failure.

## 6.2 Physical mechanisms underlying energy transfers in fragmentation

The energy transfers described previously involve two fundamental assumptions: the input energy (kinetic or potential) is fully consumed in failure, and the energy transfers only occur at the fragment scale. The first argument implies that, once a fragment is generated, it has a rigid body motion and does not vibrate elastically, which is not necessarily true. The second argument infers failure instantaneity and the absence of interactions. Indeed, in equations 17 to 22, fragment scale is assumed independent from structure scale; the equations are written in the fragment reference frame. The energy contained in a fragment only stems from its size and the value of peak stress at failure time. However, there exists an external source of energy, originating from energy exchanges between the forming fragments and the plate, and occurring during the fragmentation process. While cracks propagate and while a fragment is not fully created, it accumulates additional energy, which should appear in the energy balance. From our simulations, it is clear that fragmentation is not an instantaneous process and that dynamic effects play a key role.

Figures 8(a) and 8(b) display the time evolution of potential, kinetic, and failure energies contained in the entire plate at strain rates  $\dot{\epsilon} = 100 \text{ s}^{-1}$  and  $\dot{\epsilon} = 10^5 \text{ s}^{-1}$  for material Mat.9 (see table 1). They are typical responses at low and high strain rates, and involve very distinct mechanisms.

In both plots, since the material is elastic, potential energy first increases quadratically with time. Meanwhile, kinetic energy is constant and cohesive energy remains null. It corresponds

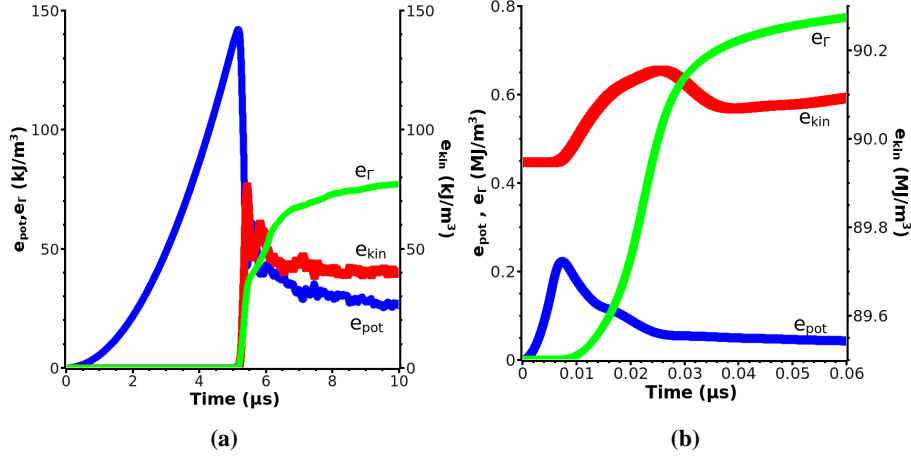


Figure 8: Time evolution of the volumetric energies for material Mat.9 (table 1). Left scale is associated to volumetric potential  $e_{pot}$  and volumetric cohesive  $e_{\Gamma}$  energies, while right scale is associated to volumetric kinetic energy  $e_{kin}$ . Strain rate is (a)  $\dot{\epsilon} = 100s^{-1}$ , and (b)  $\dot{\epsilon} = 10^5s^{-1}$ .

to the loading phase. Then, stress is high enough (compared to the cohesive strengths) and failure initiates. In the failure phase, cohesive and kinetic energy increase, whereas potential energy decreases. In comparison to the loading phase, the duration of the failure phase may vary significantly, depending on the strain rate. This results in very distinct responses.

At low strain rates (figure 8(a)), the loading phase is much longer than the failure phase. Energy variations after peak stress occur very briefly. When the loading is quasi-static, fragmentation is a highly dynamic process. Stress waves propagate very fast compared to the body motion and release quickly the structure. An extensive network of stress wave interactions establishes, and the plate undergoes a rapid and chaotic fragmentation process. The instantaneity assumption, made in energy models, is thus acceptable. However, the assumption which states that potential energy is fully converted into failure energy, is not verified. While it is true that failure energy mainly stems from potential energy and that the conversion is rapid, as highlighted by figure 8(a), potential energy is not fully employed in failure. It is also used to accelerate the fragments and increase their kinetic energies. Therefore, equation 20 provides a lower bound of the fragment size. The actual fragment size is necessarily larger than  $s_{QS}$ . In summary, when  $\dot{\epsilon} \leq \dot{\epsilon}_{TR}$ , peak potential energy (which is related to the distribution of cohesive strengths) mainly governs the amount of energy dissipated in failure. Kinetic energy at failure onset is lower than potential energy, and plays a secondary role in energy conversion processes. The distribution of cohesive strengths governs the global fragmentation response. As a result, we state that fragmentation is strength controlled.

By contrast, at high strain rates (figure 8(b)), the loading phase is briefer than the failure phase. Failure initiation is influenced by a decrease in potential energy. However, the drop is not instantaneous, as assumed in the energy models. Fragmentation is a time dependent process. The reason for this lies in the ratio between stress wave velocity and material velocity (that is proportional to the loading rate and the plate dimension). Since they are initiated almost simultaneously, defects barely undergo any stress wave effect. The stress field evolves smoothly leading to few stress wave interactions that grow independently from each other. The fragmentation process continues until stress is low enough everywhere (at least smaller than the minimum cohesive strength). Then, the energy involved in failure has released the plate from further damage evolution, and failure is completed. Moreover, it is obvious from figure 8(b) that peak potential energy is not high enough

to provide this failure energy. An additional conversion of energy takes place: kinetic energy is indirectly employed. It is used to stretch the plate, while cracks continue growing, and potential energy is constantly supplied. Since this second conversion requires time to occur, energy models do not take it into account. As a result, they underestimate fragment size. The average fragment size that we have computed confirms this interpretation (figures 7(a) and 7(b)). Therefore, when  $\dot{\epsilon} \geq \dot{\epsilon}_{TR}$ , the governing mechanism is related to the amount of energy dissipated in each microcrack, and not to the cohesive strengths values. We call it the toughness controlled regime.

## 7 Conclusion

We simulated the fragmentation of a thin plate subjected to biaxial tension, for a wide range of strain rates. A hybrid numerical framework, coupling discontinuous Galerkin and cohesive approaches, has been used. In the context of fragmentation, the main advantage of the discontinuous Galerkin framework is its ability to handle naturally discontinuities like fracture lines, and to be easily parallelized. Cohesive elements are activated dynamically, as soon as local stress reaches the cohesive strength. By defining Weibull distributions of cohesive strengths, we modeled the micro-structural heterogeneity of the material. Varying the parameters used in the material parameters (Young's modulus, volumetric mass, toughness, minimum cohesive strength, scale parameter, and Weibull modulus) allowed us to quantify their influence on fragmentation. We tackled the issue of convergence and showed that, for fine enough meshes, the number of fragments, and the distribution of fragment masses are independent from the number of degrees of freedom.

The study of the average fragment size and its comparison to energy models has revealed the prevailing role of the dynamics of stress waves and energy transfer in fragmentation. First, we observed that, although the average fragment size is highly dependent upon material parameters, an adequate scaling gathered the scattered responses into a reasonable trend. Also valid in one-dimension, this general response is characteristic of the fragmentation of a heterogeneous plate loaded in biaxial tension. It highlights the limitations of energy models, as well as the existence of two regimes, the strength and the toughness controlled regimes. The transition has been derived analytically as a function of material properties.

The strength controlled regime occurs at low and intermediate strain rates. It is dominated by the quasi-instantaneous conversion of potential energy into failure energy. The extensive network of stress waves accompanies this highly dynamic fragmentation response, and few fragments are generated. The toughness controlled regime is characterized by a relatively longer fragmentation response, and occurs at high strain rates. Since stress waves propagate at a speed close to the material point velocities, defects barely undergo any stress wave effect. They do not interact as much with each other and damage evolves smoothly. Both kinetic and potential energy are employed in failure. In this toughness controlled regime, the amount of dissipated energy prevails, irrespective of the cohesive strengths values. Future work will extend these energetic considerations to a broader class of loading conditions, including impacts.

## Acknowledgments

The authors gratefully acknowledge the support from ARO through the grant number W911NF-08-1-0150, and ARL through University of Nebraska Lincoln (grant number W911NF-04-2-0011). RR gratefully acknowledges the partial support of LSMS during his sabbatical stay at

EPFL, of the US Army through the Institute for Soldier Nanotechnologies, under Contract DAAD-19-02-D-0002 with the US Army Research Office; as well as support of the Office of Naval Research under grant N00014-07-1-0764.

## References

- [1] G.T. Camacho and M. Ortiz. Computational modelling of impact damage in brittle materials. *International Journal of Solids and Structures*, 33(20-22):2899–2938, 1996.
- [2] N.P. Daphalapurkar, K.T. Ramesh, L. Graham-Brady, and J.F. Molinari. Predicting variability in the dynamic failure strength of brittle materials considering pre-existing flaws. *Journal of the Mechanics and Physics of Solids*, In Press, Accepted Manuscript:–, 2010.
- [3] C. Denoual, G. Barbier, and F. Hild. A probabilistic approach for fragmentation of brittle materials under dynamic loading. *Mechanics of Solids and Structures*, t.325, Serie II b:685–691, 1997.
- [4] W.J. Drugan. Dynamic fragmentation of brittle materials: analytical mechanics-based models. *Journal of the mechanics and physics of solids*, 49(6):1181–1208, 2001.
- [5] L.A. Glenn and A. Chudnovsky. Strain-energy effects on dynamic fragmentation. *Journal of Applied Physics*, 59(4):1379–1380, 1986.
- [6] D.E. Grady. Local inertial effects in dynamic fragmentation. *Journal of Applied Physics*, 53(1):322–325, 1982.
- [7] D.E. Grady and M.E. Kipp. Experimental measurement of dynamic failure and fragmentation properties of metals. *International Journal of Solids and Structures*, 32(17-18):2779 – 2791, 1995.
- [8] Dennis Grady. *Fragmentation of Rings and Shells, The Legacy of N.F. Mott*. Springer, 2010.
- [9] D.L. Grote, S.W. Park, and M. Zhou. Dynamic behavior of concrete at high strain rates and pressures:i. experimental characterization. *International Journal of Impact Engineering*, 25:869–886, 2001.
- [10] S. Levy and J.F. Molinari. Dynamic fragmentation of ceramics, signature of defects and scaling of fragment sizes. *Journal of the Mechanics and Physics of Solids*, 58(1):12–26, 2010.
- [11] J.F. Molinari, G. Gazonas, R. Raghupathy, A. Rusinek, and F. Zhou. The cohesive element approach to dynamic fragmentation: The question of energy convergence. *International Journal for Numerical Methods in Engineering*, 69:484–503, 2007.
- [12] N.F. Mott. Fragmentation of shell cases. *Royal society. London series A-mathematical and physical Sciences*, 189:300–308, 1947.
- [13] N.F. Mott and E.H. Linfoot. A theory of fragmentation. *Ministry of Supply*, AC3348, 1943.
- [14] J.A. Nitsche. Über ein variationsprinzip zur losung dirichlet-problemen bei verwendung von teilraumen, die keinen randbedingungen uneworfen sind. *Abhandlungen aus dem Mathematischen Seminar der Universität Hamburg*, 36:9–15, 1971.



- [15] L. Noels and R. Radovitzky. A general discontinuous galerkin method for finite hyperelasticity. formulation and numerical applications. *International Journal for Numerical Methods in Engineering*, 68:64–97, 2006.
- [16] L. Noels and R. Radovitzky. An explicit discontinuous galerkin method for non-linear solid mechanics: Formulation, parallel implementation and scalability properties. *International Journal for Numerical Methods in Engineering*, 74:1393–1420, 2008.
- [17] R. Radovitzky, A. Seagraves, M. Tupek, and L. Noels. A scalable 3d fracture and fragmentation algorithm based on a hybrid, discontinuous galerkin, cohesive element method. *Computer Methods in Applied Mechanics and Engineering*, 200(1-4):326 – 344, 2011.
- [18] A. Seagraves and R. Radovitzky. *Dynamic Failure of Materials and Structures, chapter Advances in Cohesive Zone Modeling of Dynamic Fracture*. Springer, 2009.
- [19] V.B. Shenoy and K.S. Kim. Disorder effects in dynamic fragmentation of brittle materials. *Journal of the Mechanics and Physics of Solids*, 51:2023–2035, 2003.
- [20] C.J. Shieh, V.F. Nesterenko, and M.A. Meyers. High strain rate deformation and comminution of silicon carbide. *Journal of Applied Physics*, 83:4660–4671, 2000.
- [21] W. Weibull. A statistical theory of strength of materials. *Generalstabens Litografiska Anstalts Förlag*, page 151, 1939.
- [22] F.K. Wittel, F. Kun, H.J. Herrmann, and B.H. Kroplin. Breakup of shells under explosion and impact. *Physical Review E*, 71(1):016108, 2005.
- [23] F. Zhou, J.F. Molinari, and K.T. Ramesh. Characteristic fragment size distributions in dynamic fragmentation. *Applied Physics Letters*, 88(261918), 2006.
- [24] F. Zhou, J.F. Molinari, and K.T. Ramesh. Effects of material properties on the fragmentation of brittle materials. *International Journal of Fracture*, 139(2):169–196, 2006.